Nanoscale

PAPER

View Article Online
View Journal | View Issue

Cite this: *Nanoscale*, 2017, **9**, 907

Micro-structured inverted pyramid texturization of Si inspired by self-assembled Cu nanoparticles

Yan Wang,[a,b] Yaoping Liu,*[a] Lixia Yang,[a] Wei Chen,[a] Xiaolong Du[a] and Andrej Kuznetsov*[b]

Received 17th October 2016,
Accepted 4th December 2016

DOI: 10.1039/c6nr08126f

www.rsc.org/nanoscale

A superior micron-sized inverted pyramid structure has been successfully achieved by one-step copper nanoparticles assisted chemical etching in $Si/Cu(NO_3)_2/HF/H_2O_2$ solution for light trapping in silicon solar cells. The detailed mechanisms of such a novel method have been systematically demonstrated. The charge transfer during the reaction has been revealed by the simplified energy band diagram of the system as well. In order to form micro-structured inverted pyramids, the generation and dissolution of Cu nanoparticles should keep in balance during the reaction, which depends on the concentration of the etchant, the doping type and the doping level of the silicon substrate. With the investigation of the intrinsic properties of the silicon substrate, the etching rate is found out as a combined result of the electron concentration and the defect density of the substrate, as well as the potential barrier on the interface of Si/Cu nanoparticles. Furthermore, the anisotropic nature of Cu assisted chemical etching has also been investigated.

Introduction

Black silicon has drawn a lot of attention in recent years because of its extensive application in fields such as solar cell energy conversion,[1–3] thermal power conversion,[4] energy storage,[5] chemical and biological sensing,[6] and so on. It has been proposed as an ideal material for photovoltaics due to its outstanding light management properties in the solar spectrum which benefits from a gradually changed reflective index at the silicon/air interface.[7,8] So far, metal assisted chemical etching (MACE) is one of the most popular methods to fabricate nanostructured black silicon because of its good controllability and low cost.[9,10] Meanwhile, MACE has also been proposed as an effective method to texture multicrystalline diamond wire sawn silicon wafers which can't be uniformly textured by conventional acid methods.[11] In a typical MACE procedure, a silicon substrate, partly covered by noble metal nanoparticles (NPs) such as Pt, Au, and Ag by electroless or vacuum deposition, is immersed into an aqueous solution composed of HF and an oxidative agent (usually H_2O_2). The Si beneath the noble metal NPs is etched much faster than the bare region, resulting in the formation of nanostructures. Currently, Ag nanoparticles (NPs) are the most widely adopted noble metals to catalyze the etching of silicon because of their relatively low cost and simple process.[12,13] However, even with one-step Ag assisted chemical etching (AACE), silicon wafers should be pre-treated in order to avoid raw damage, which complicates the procedure and increases the cost as well. Moreover, there are also remaining issues identified as serious bottlenecks for such nanostructured black silicon solar cells, in particular lifetime degradation in combination with the formation of an excess "dead layer" in the emitter rising from the increased surface area and doping concentration,[14] which limits the performance of the device.

Recently, copper has been employed as an electrode material instead of Ag in order to reduce the cost of silicon solar cells.[15,16] As a widely used metal in commercial Si microfabrication facilities, Cu impurities had been suggested to be less detrimental to the silicon solar cell performance than Au and Ag.[17] However, early work had figured out that Cu NPs were not ideal for MACE of silicon. Unlike electroless deposition of Ag NPs during AACE, compact and continuous Cu films were usually formed on the silicon substrate in the solution of copper ions and HF, which isolated Si from the etchant and resulted in the termination of the etching process.[18,19] On the other hand, in the case of the existence of other oxidants (*e.g.* H_2O_2 and Fe^{3+}), Cu NPs can be oxidized and vanished immediately after a short-time incubation in the etchant due to the low redox potential of Cu^{2+}/Cu,[20,21] forming only shallow pits which limit the effectiveness as an anti-reflective layer. Y. T. Lu *et al.* firstly reported Cu assisted chemical

[a]*Key Laboratory for Renewable Energy, Beijing Key Laboratory for New Energy Materials and Devices, National Laboratory for Condensed Matter Physics, Institute of Physics, Chinese Academy of Sciences, Beijing, 100190, China. E-mail: ypliu@iphy.ac.cn*
[b]*Department of Physics, University of Oslo, Oslo, 0316, Norway. E-mail: andrej.kuznetsov@fys.uio.no*

etching (CACE) to fabricate a nanopore-type antireflective layer.[22] Subsequently, F. Toor *et al.* achieved nanostructured black silicon fabricated by CACE, demonstrating a more potential method than Au or Ag assisted chemical etching.[23] Very recently, Y. Cao *et al.* have figured out that the mechanism of CACE was quite different from typical MACE because there are no Cu NPs observed during the etching process.[24]

We fabricated micron-sized "inverted pyramid" structures by maskless CACE, which realized real one-step etching of raw silicon wafers without any pre-treatment, greatly reduced the cost and simplified the procedure.[25,26] The inverted pyramid texture, employed by the highest-efficiency passivated emitter with rear locally diffused (PERL) cells, outperformed the pyramid texture and black silicon because of their superior light-trapping and structure characteristics.[27–29] Our one-step method gives an opportunity for inverted pyramids to be free from complex techniques involving lithography, laser processes, *etc.*, and fulfill the industrial application.[30–32] The mechanism of inverted pyramid fabrication by CACE was quite different from the few existing literature methods. In this paper, we systematically demonstrated the mechanism of CACE of silicon in $Cu(NO_3)_2/HF/H_2O_2$ aqueous solution. The details of the CACE process are presented by the energy band diagrams of the $Si/Cu(NO_3)_2/HF/H_2O_2$ system before and after equilibration. As a key role, the dynamics of Cu NPs was discovered by two-step CACE. The etching kinetics was investigated in the samples exhibiting different surface morphologies, crystal orientations and carrier concentrations, as well as different concentrations of the etchant.

Experimental

(100)-oriented crystalline silicon (c-Si) wafers of p-type (phosphorus-doped, resistivity 0.001–0.005 Ω cm, 1–20 Ω cm, or 5000–6000 Ω cm) and n-type (boron-doped, resistivity 0.01–0.02 Ω cm, 1–10 Ω cm, or 10 000–12 000 Ω cm) with different surface morphologies (raw, KOH polished, and polished) were employed. Before being etched, samples were ultrasonically cleaned with a sequential acetone and ethanol bath to remove any organic contaminants, and then rinsed with deionized water. Cu assisted chemical etching of silicon took place in a polytetrafluoroethylene container at 50 °C with various concentrations of $Cu(NO_3)_2$, H_2O_2 and HF. Residual Cu NPs were removed away using concentrated nitric acid in a sonication bath for at least 20 min. The silicon wafers were thoroughly rinsed with deionized water and dried under flowing nitrogen. The morphologies and structures of the samples were characterized by using a scanning electron microscope (SEM). The average etching rate (R_{av}) was calculated as:[24]

$$R_{av.} = \frac{\Delta m}{2\rho_{Si} S t}$$

where Δm is the mass loss of the sample, ρ_{Si} is the mass density of crystalline silicon, S is the silicon surface area, and t is the etching time.

Results and discussion

Fig. 1 shows the top and cross sectional SEM images of commercial 156 mm × 156 mm, boron-doped (1–3 Ω cm), (100)-oriented c-Si wafers after being etched in the 5 mM $Cu(NO_3)_2$, 4.6 M HF and 0.55 M H_2O_2 mixture for 15 min at 50 °C. Random inverted pyramids with sizes of 2–6 μm can be observed over the whole wafer (Fig. 1a). As can be observed from Fig. 1b, Cu NPs were left on the surface of the inverted pyramid, the density of which increased from the top to the bottom of the inverted pyramid. With the inverted pyramid texture, the average reflectivity of the silicon wafer in the wavelength range from 300 nm to 1000 nm can be reduced as low as 5%, which is much lower than the conventional pyramid texture (Fig. 2), and periodic inverted pyramids as well.[33] When light illuminates on the pyramid structure, it will collide twice on the surface. As with the inverted pyramid structure, 37% of the incident light will undergo triple bounce, which increases the path length, enhances the interaction with silicon and finally improves the light trapping ability of the silicon wafer.[28]

The general etching process of CACE was like typical one-step MACE, in which Cu NPs were electrolessly deposited onto the silicon substrate's surface when immersing silicon into the enchant and then catalyzed the etching of silicon with

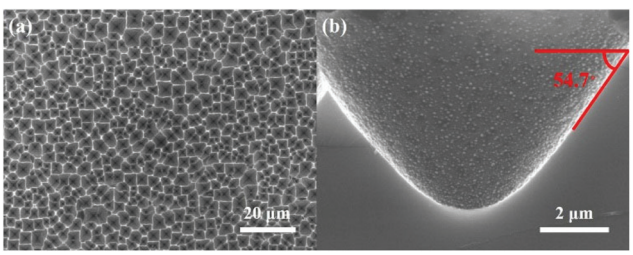

Fig. 1 SEM images of commercial boron-doped (1–3 Ω cm), (100)-oriented c-Si wafers after being etched in the 5 mM $Cu(NO_3)_2$, 4.6 M HF and 0.55 M H_2O_2 mixture for 15 min at 50 °C. (a) Top SEM; (b) cross sectional SEM.

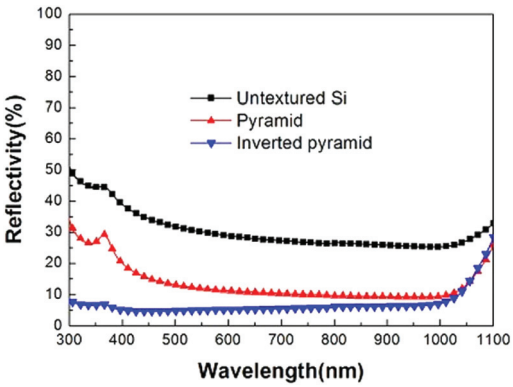

Fig. 2 Reflectance spectra of silicon wafers with no texture, conventional pyramid texture, inverted pyramid texture fabricated by CACE.

HF and H_2O_2. The reaction can be described as two half-cell reactions:[24,25,34]

Cathode reaction:

$$Cu^{2+} + 2e^- \rightarrow Cu^0(s) \quad E_0 = +0.34 \text{ V per SHE} \tag{1}$$

$$H_2O_2 + 2H^+ \rightarrow 2H_2O + 2h^+ \quad E_0 = +1.76 \text{ V per SHE} \tag{2}$$

Anode reaction:

$$Si(s) 6HF + nh^+ \rightarrow H_2SiF_6 + nH^+ + \frac{4-n}{2}H_2 \uparrow \quad E_0 = -1.20 \text{ V per SHE} \tag{3}$$

where SHE is the standard hydrogen electrode, n is the number of holes per dissolved Si atom. In this case, Cu NPs act as a microscopic cathode on which the reduction of the oxidant occurs (cathode reactions (1) and (2)). Simultaneously, at the anode, silicon beneath the Cu NPs is oxidized and then dissolved with HF.

The driving force of charge exchange is the difference between the redox potentials of redox species in solution and the Fermi level of silicon.[32] The redox potential at equilibrium of the electrochemical reaction (eqn (1) and (2)) can be estimated by the Nernst relationship as follows:

$$E_{Cu}(\text{V per SHE}) = 0.34 + \frac{RT}{2F}\ln[Cu^{2+}] \tag{4}$$

$$E_{H_2O_2}(\text{V per SHE}) = 1.76 + \frac{RT}{F}\ln[H^+] \tag{5}$$

in which E is the equilibrium potential, R is the ideal-gas constant 8.314 J kmol^{-1}, F is the Faraday constant 96 500 C mol^{-1}, T is the absolute temperature, $[Cu^{2+}]$ and $[H^+]$ are the molarities of Cu^{2+} and H^+ in the solution, respectively. The dissociation constants of HF and H_2O_2 are assumed to be about $K_{a_{HF}} = 6.8 \times 10^{-4}$ and $K_{a_{H_2O_2}} = 2.2 \times 10^{-12}$ at approximately room temperature. Thus, the concentration of H^+ can be calculated to be about 5.56×10^{-2} M. The equilibrium potential of H_2O_2 can then be obtained as 1.68 V. In the HF/H_2O_2 solution, if the concentration of Cu^{2+} is assumed to be 5×10^{-3} M, the equilibrium potential of Cu^{2+} can be calculated to be about 0.20 V.

Fig. 3a displays the simplified energy band diagrams before and after equilibration when immersing p-type silicon into Cu$(NO_3)_2$/HF/H_2O_2 solution. The redox potentials of Cu^{2+}/Cu and H_2O_2/H_2O indicated in the energy diagram are expressed with respect to a value of −4.50 eV for the standard hydrogen electrode.[32] When the silicon wafer was immersed into the etchant, Cu^{2+} could capture electrons from the silicon conduction band, be oxidized and deposited on the silicon surface as Cu nuclei where the interface became a semiconductor/metal contact. As the Fermi level of p-Si was lower than the work function of Cu, the majority carrier (holes) of silicon at the interface would be depleted, and both the conduction band and valence band would bend downwards. The energy band diagram after equilibration indicated that the charge transformation occurred near the Si/Cu interface. The electrons from the Si conduction band could jump down to Cu nuclei and then be obtained by Cu^{2+} or H_2O_2, resulting in the growth of Cu NPs or the reduction of H_2O_2. Simultaneously, the holes were injected into the valence band of Si through Cu, leading to the oxidization of Si and the dissolution of Si by HF. As a result, silicon beneath the Cu NPs was etched and Cu NPs sank into the shallow pits on the silicon surface.

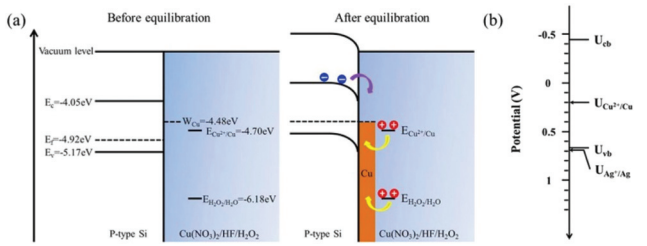

Fig. 3 (a) Simplified energy band diagrams before and after equilibration when immersing p-type silicon into Cu$(NO_3)_2$/HF/H_2O_2 solution. (b) Qualitative diagram of the comparison between the electrochemical electron energy levels of the Si band edges (E_c and E_v are the conduction and valence bands, respectively) and redox couples, such as Cu^{2+}/Cu and Ag^+/Ag, in HF solution.

Notably, in the overall corrosion reaction, *i.e.*, the copper deposition process, both electron capture (reduction of copper ions) and hole injection (oxidation of Si) are required. However, as the redox potential of Cu^{2+}/Cu lies well above the valence band of Si, the hole injection into the silicon valence band becomes difficult. That's the reason why CACE of silicon is hard to proceed at room temperature and the solution should be heated up in order to accumulate the etching rate which is different from the well-investigated AACE. In the case of AACE, as the energy levels of Ag^+/Ag redox couples overlap with the valence band of silicon (Fig. 3b), hole injection becomes more likely and the reduction of Ag^+ ions is not limited by the concentration of minority carriers.[35]

The etching rate of CACE positively correlates with the current density (j_c) of the associated redox process, expressed as follows for p-type Si:[36,37]

$$j_c = zek_c n_s C_{redox} \exp(-U_c/k_B T) \tag{6}$$

where z is the number of electrons transferred during the reaction, e is the charge of electrons, k_c is the rate constant, n_s is the electron density at the interface, C_{redox} is the concentration of the oxidant at the interface, U_c is the activation energy for the cathodic reaction, k_B is the Boltzmann constant, and T is the absolute temperature. A similar equation holds for n-type Si. Although the H_2O_2/H_2O redox couple has a much higher redox potential than the valence band of silicon, the reaction of silicon etching is very slow without Cu NPs. In this case, the catalytic activity of Cu NPs can be interpreted as the decrease of the activation energy U_c. As can be observed from eqn (6), the j_c also shows high dependence on the electron density and oxidant concentration at the interface.

Fig. 4 presents the SEM images of c-Si (100), boron-doped (1–3 Ω cm), after being etched in the 5 mM Cu$(NO_3)_2$, 4.6 M HF and 0.55 M H_2O_2 mixture for 5 min and 10 min, respectively. Cu NPs with sizes ranging from 10 nm to 20 nm distributed on the inverted pyramid surface. With the prolongation of

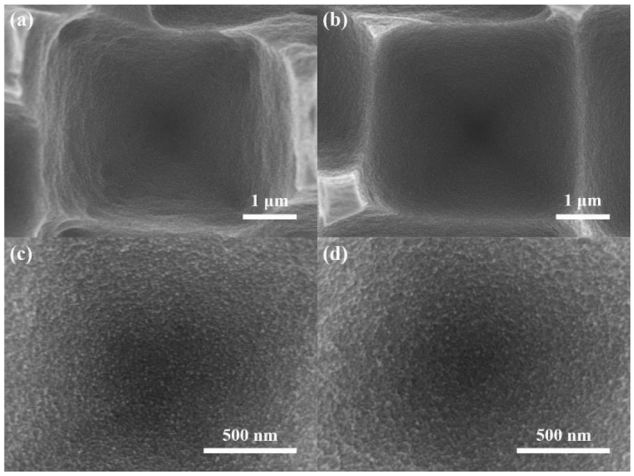

Fig. 4 SEM images of c-Si (100), boron-doped (1–3 Ω cm), after being etched in the 5 mM $Cu(NO_3)_2$, 4.6 M HF and 0.55 M H_2O_2 mixture at 50 °C for 5 min and 10 min, respectively. (a) 5 min; (b) 10 min; (c) and (d) are the magnified SEM images of (a) and (b) respectively.

the etching time, no visible changes in either the size or the density of the Cu NPs were observed, which was the key point in the case of successful fabrication of an inverted pyramid structure. A conclusion can be made that the number and size of the Cu NPs should keep in a certain range in order to well control the etching rate. Two possibilities can be drawn about the Cu NPs: (i) when the number of Cu NPs reach a certain value, Cu NPs stop generating; (ii) the Cu NPs reach dynamic equilibrium, *i.e.* the generation and dissolution of Cu NPs remain in balance during the reaction.

In order to determine the activity of Cu NPs, commercial boron-doped (1–3 Ω cm) c-Si (100) was firstly deposited with the Cu film with 3 nm thickness on one side by thermal evaporation, and then immersed into the 4.6 M HF and 0.55 M H_2O_2 mixture for 15 min.[38] Cu NPs with a size around 10 nm covered only on one side of the silicon wafer after the deposition of the 3 nm Cu film (Fig. 5a). After being immersed into the 4.6 M HF and 0.55 M H_2O_2 mixture for 15 min, the deposited Cu NPs disappeared, which indicated that the Cu NPs were oxidized by H_2O_2 in the solution. Synchronously, nanostructures were formed on both sides of the silicon surface (Fig. 5b and c). Since the redox potential of H_2O_2/H_2O was much higher than Cu^{2+}/Cu, Cu NPs could obtain holes from H_2O_2 and then be oxidized and dissolved. Notably, similar nanostructures were found on the other side of the silicon wafer which had no original Cu NPs deposition. This finding can show clearly that the Cu NPs were oxidized to Cu^{2+} by the hole injection from H_2O_2, and then the Cu^{2+} ion in the solution could obtain electrons from the silicon conduction band, deposit on the other side of the silicon wafer again and catalyze the etching of silicon. The activities of the Cu NPs can be expressed by the chemical reaction as eqn (7) and (1).

$$Cu + H_2O_2 + 2H^+ \rightarrow 2H_2O + Cu^{2+} \quad (7)$$

A conclusion can be made that the generation and dissolution of Cu NPs reached dynamic equilibrium during the inverted pyramid structure formation.

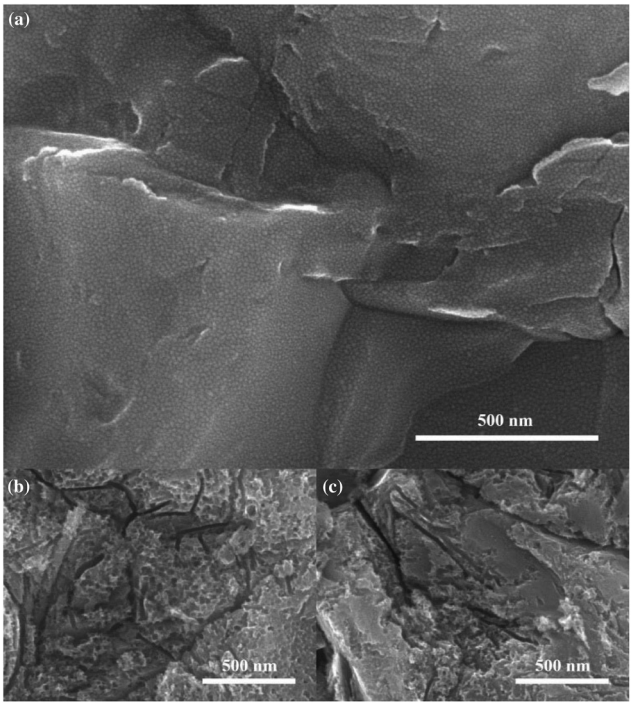

Fig. 5 (a) SEM image raw silicon wafer with a 3 nm Cu film; (b) and (c) SEM images of the Cu deposited side and the non-Cu deposited side of the silicon wafer after being immersed into the 4.6 M HF and 0.55 M H_2O_2 mixture for 15 min.

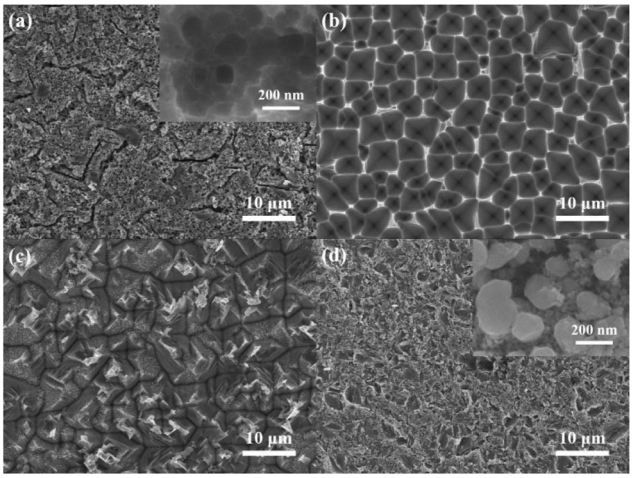

Fig. 6 SEM images of commercial boron-doped (1–3 Ω cm), c-Si (100) wafers after being etched in 5 mM $Cu(NO_3)_2$, 4.6 M HF and H_2O_2 with a varied concentration for 15 min at 50 °C. (a) H_2O_2 0.66 M, (b) H_2O_2 0.55 M, (c) H_2O_2 0.44 M, and (d) H_2O_2 0.00 M.

As discussed above, the density of the Cu NPs is the key point of inverted pyramid structure fabrication, which relates to the concentration of the etchant. Fig. 6 shows the SEM images of the commercial boron-doped (1–3 Ω cm), c-Si (100) wafers after being etched in the $Cu(NO_3)_2/HF/H_2O_2$ mixture with varied H_2O_2 concentration for 15 min. With a high concentration of H_2O_2 (0.66 M) (Fig. 6a), the surface of the silicon

substrate appeared as porous silicon. A high H_2O_2 concentration would accelerate the reaction expressed as eqn (7). H_2O_2 injected holes to Cu NPs immediately when Cu NPs were deposited on the silicon surface, leading to the complete disappearance of Cu NPs. The etched structure was shallow because of the low lifetime of Cu NPs. When came to the next circle, the reduction of the Cu^{2+} ion probably didn't take place at exactly the same position as before, which disabled the continuous etching of silicon and finally resulted in the formation of porous silicon. When the concentration of H_2O_2 decreased to 0.55 M, the generation of Cu NPs by electroless deposition and the dissolution of Cu NPs by H_2O_2 reached equilibrium, leading to the anisotropic etching of silicon to form inverted pyramid structures (Fig. 6b). The lack of H_2O_2 from the balanced value would lead to the increase of Cu NPs and then the destruction of inverted pyramid structures. As the H_2O_2 concentration decreased to 0.44 M, the size of Cu NPs became bigger which can be observed by the naked eye (Fig. 6c). Furthermore, when H_2O_2 was absent in the etching solution, a thick Cu film was deposited on the silicon surface (Fig. 6d). As there's no other oxidant in the solution, Cu NPs couldn't be oxidized and dissolved when deposited on the silicon surface. With the growth of Cu NPs, a compact Cu film formed, which insulated the solution and the silicon and slowed down the reaction rate. In this case, Cu NPs didn't exhibit the anisotropic etching ability, and the reaction can be described by using eqn (1) and (3). Notably, the lack or excess of Cu^{2+} ions can also lead to a similar result.

According to eqn (6), the etching rate of CACE depends not only on the concentration of the etchant, but also on the doping type and doping level of silicon substrates. Fig. 7 shows the SEM images of both polished p-type (boron doped, 0.001–0.005 Ω cm, 1–10 Ω cm, 5000–6000 Ω cm) and n-type (phosphorus doped, 0.01–0.02 Ω cm, 1–10 Ω cm, 10 000–12 000 Ω cm) c-Si (100) after being etched in the 5 mM $Cu(NO_3)_2$, 4.6 M HF and 0.55 M H_2O_2 mixture for 15 min at 50 °C. The surface morphology varied from each other. For highly doped p-Si (0.001–0.005 Ω cm), shallow micron-sized pits uniformly distributed on the silicon surface (Fig. 7a and b). As the doping level was high, tiny pores could be observed on the surface of inverted pyramids (the insert figure of Fig. 7a).[39] With the decrease of B doping concentration, the etched pits deepened and transformed to inverted pyramids (Fig. 7c). However, only some regions were etched, the others were still left as polished (Fig. 7d). The non-etched regions reduced when the resistance of p-Si increased to 5000–6000 Ω cm (Fig. 7f). In the meantime, the inverted pyramids became more uniform (Fig. 7e). It should be mentioned that with the resistance of the p-Si wafer increasing, the concentration of defects which were induced by the dopant decreased, while the concentration of minority carriers (electrons) increased. As the electroless deposition of metal nanoparticles, such as Ag and Cu, preferred to take place at defective sites,[40] high concentrations of defects would help to speed up the etching rate. On the other hand, according to the discussion above, the electron transfer from the silicon conduction band was required to guarantee the proceeding of the reaction. Thus, the higher concentration of electrons would facilitate the etching process. In the case of highly doped p-Si, the defective sites were many enough to distribute over the whole wafer,

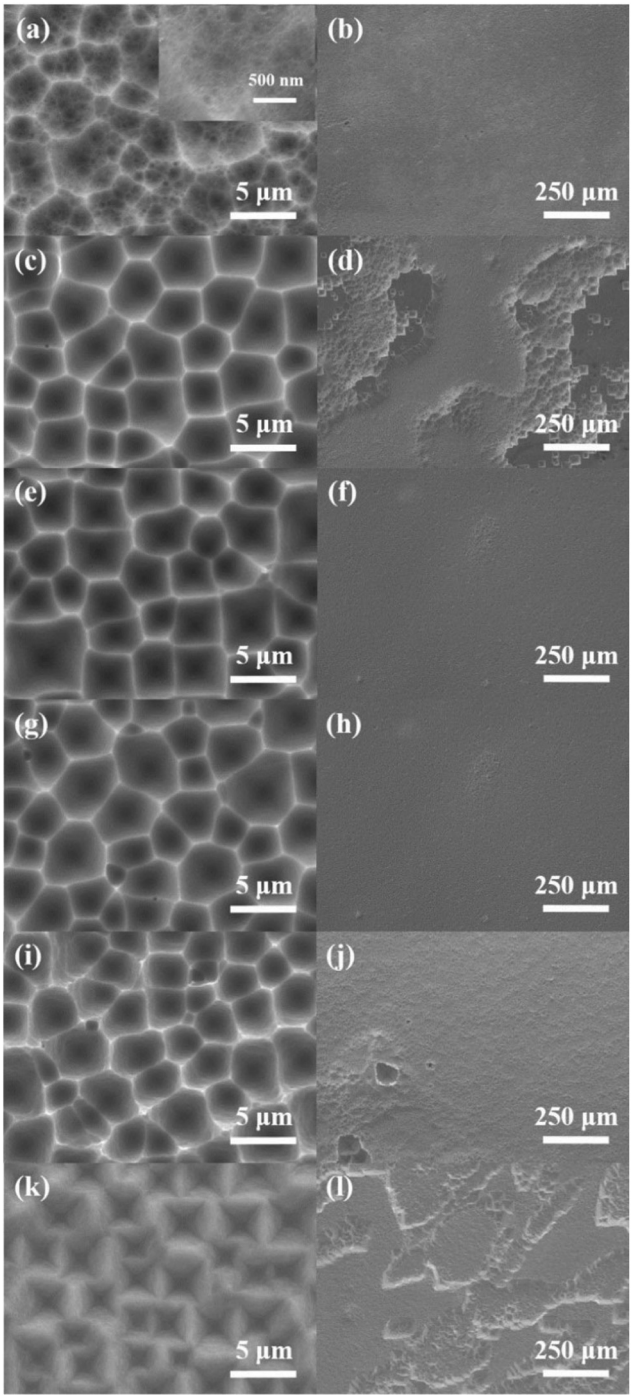

Fig. 7 SEM images of polished c-Si (100) wafers with different doping types and doping concentrations after being etched in the 5 mM $Cu(NO_3)_2$, 4.6 M HF and 0.55 M H_2O_2 mixture for 15 min at 50 °C. (a), (b) p-Si, 0.001–0.005 Ω cm; (c), (d) p-Si, 1–10 Ω cm; (e), (f) p-Si, 5000–6000 Ω cm; (g), (h) n-Si, 10 000–12 000 Ω cm; (i), (j) n-Si, 1–10 Ω cm; (k), (l) n-Si, 0.01–0.02 Ω cm.

so the silicon substrate could be uniformly etched. However, due to the lack of electrons, the deposition of Cu NPs was limited, resulting in shallow pits. For silicon with 1–10 Ω cm resistance, the increased electrons accelerated the formation of inverted pyramid structures, while the reduced defects made a decrease of starting points and then led to the partial etching of Si. As to the lightly doped one (5000–6000 Ω cm), the concentration of minority carriers was high enough to offset the lack of defective sites, making the etching morphology more uniform than the one with 1–10 Ω cm resistance. Different from p-type Si, the n-type silicon wafers with varied resistance more or less formed Cu NPs which can be observed by the naked eye. With the decrease of resistance, more and more Cu NPs emerged on the silicon surface, and finally formed large and deep inverted pyramid-like structures (Fig. 7g–l). Contrary to p-type Si, the defect concentration and electron concentration increased simultaneously when decreasing the resistance, which enhanced the etching rate and led to the deposition of excessive Cu NPs.

The average etching rate of the samples discussed above is displayed in Fig. 8a. With the increase of electron concentration, the average etching rate first decreased a bit and then increased gradually. Notably, in the case of p-type Si with 1–10 Ω cm resistance, the real etching rate of the etched region should be higher than the one with 0.001–0.005 Ω cm resistance; as there's still some region left unetched, the average etching rate decreased.

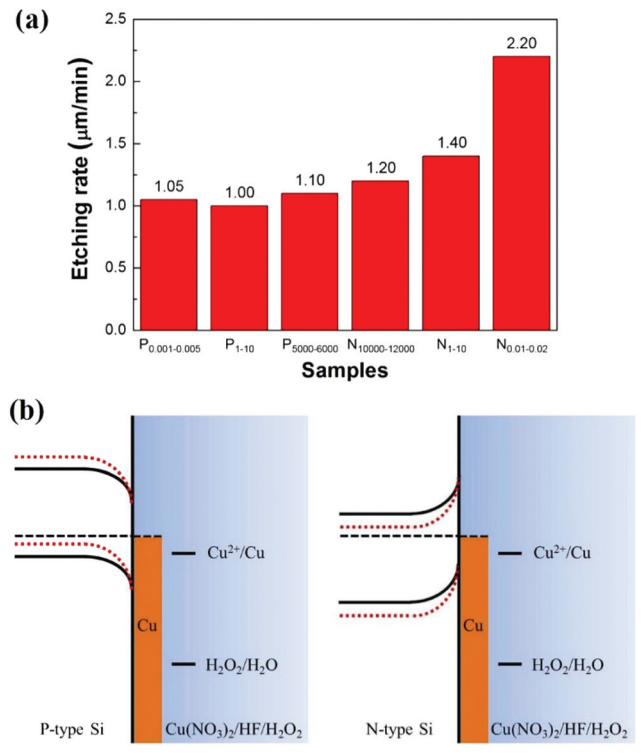

Fig. 8 (a) The average etching rate of silicon wafers with different doping types and concentrations. (b) Simplified energy band diagrams after equilibration when immersing lightly doped (solid) or highly doped (dashed) p-type (left) or n-type (right) silicon into $Cu(NO_3)_2/HF/H_2O_2$ solution.

Fig. 8b shows the simplified energy band diagrams after equilibration when immersing lightly doped (solid) or highly doped (dash) p-type and n-type silicon into the $Cu(NO_3)_2/HF/H_2O_2$ solution. When contacted with the deposited Cu NPs, the majority carriers of silicon at the interface were depleted, and both the conduction band and valence band would bend. The higher the doping level, the larger the bending. The energy band bent downwards for p-Si, while bent upwards for n-Si. For highly boron doped silicon, the large bending would make the electrons more easy to collect by Cu NPs. The etching rate was limited by the concentration of minority carriers. In the case of n-type silicon, the potential barrier of the electrons was higher for the heavily doped ones. The relationship between the doping concentration N_D and the width of the space-charge region (SCR) could be written as:[41]

$$w_{SCR} = \sqrt{\frac{2 \in \in_0 (U_B - U)}{eN_D}}. \quad (8)$$

Herein, $\in_0$ is the permittivity of the vacuum, $\in$ is the permittivity of the material (for Si is 11.9), U_B is the barrier height, U is the applied bias in the forward direction and N_D is the doping concentration. The U is 0 V, and U_B is expressed as follows:[42]

$$U_B = \phi_{mCu} - \chi_{Si} - \frac{1}{2}E_{gSi} + kT \ln\left(\frac{N_D}{n_i}\right) \quad (9)$$

where ϕ_{mCu} is the work function of Cu, χ_{Si} is the electronic affinity of Si, E_{gSi} is the band gap of Si, and n_i is the intrinsic electron concentration in silicon. Thus, eqn (8) can be written as:

$$w_{SCR} = \sqrt{\frac{2 \in \in_0 \left[\phi_{mCu} - \chi_{Si} - 1/2E_{gSi} + kT \ln(N_D/n_i)\right]}{eN_D}}. \quad (10)$$

According to eqn (10), the larger the doping concentration N_D, the narrower the potential barrier. When the doping concentration reaches above 1×10^{18} atoms per cm^3, the electrons may tunnel. In the case of n-type silicon with a resistance of 0.01–0.02 Ω cm, the doping concentration is more than 1×10^{18} atoms per cm^3, the electrons can easily tunnel through the narrow potential barrier, and then be obtained by the oxidant in solution. That's the reason why its etching rate was much higher than the other two n-type Si samples.

In order to further confirm the defects' effect on CACE, silicon wafers with different surface morphologies were etched in $Cu(NO_3)_2/HF/H_2O_2$ solution. Fig. 9 shows the SEM images of raw, KOH polished and polished c-Si (100) wafers with similar resistance etched in the 5 mM $Cu(NO_3)_2$, 4.6 M HF and 0.55 M H_2O_2 mixture at 50 °C for 1 min, 2 min, and 3 min. At the first 1 minute, the differences among the silicon wafers with different original surface morphologies were extremely obvious. The reaction of raw silicon wafer was vigorous when immersed into the solution, and the original raw damage

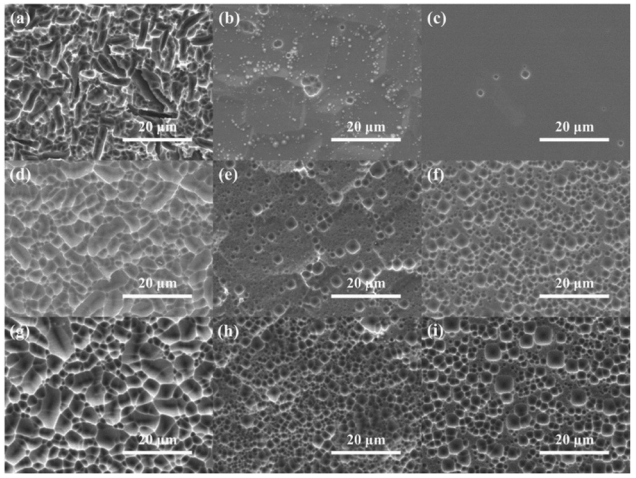

Fig. 9 SEM images of c-Si (100) wafers with different surface morphologies etched in the 5 mM $Cu(NO_3)_2$, 4.6 M HF and 0.55 M H_2O_2 mixture at 50 °C for different times. (a), (d), (g) Raw Si, etched for 1 min, 2 min, and 3 min respectively; (b), (e), (h) KOH polished Si, etched for 1 min, 2 min, and 3 min respectively; (c), (f), (i) polished Si, etched for 1 min, 2 min, and 3 min respectively.

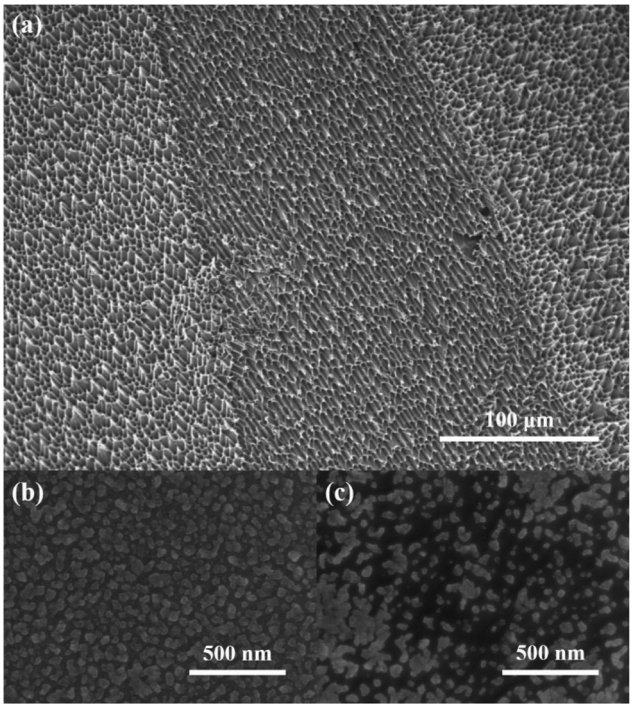

Fig. 10 (a) SEM image of the mc-Si wafer etched in $Cu(NO_3)_2/HF/H_2O_2$ solution for 15 min. (b) and (c) SEM images of the Si (100) and Si (111) wafers after being immersed in 5 mM $Cu(NO_3)_2$ and 4.6 M HF mixed solution at 50 °C for 20 s.

almost disappeared in 1 min. As to the KOH polished one, only several inverted pyramids were found at the edge of the steps where there's a higher density of defects, indicating that the CACE preferred to start at the defective sites.[43,44] For the polished silicon wafer, there're even less inverted pyramids, since the surface was completely polished and had less defects. The weaker Si–Si bond at the defect region made the electrons easier to be collected by the oxidant in the solution, leading to the prior reaction in these areas. With the prolongation of reaction time, the region without defects could also be etched. Finally, the difference among these samples became small.

The formation of inverted pyramids mainly depends on the anisotropic etching between the Si (111) and other planes. Fig. 10a shows an SEM image of a multicrystalline silicon (mc-Si) wafer etched in $Cu(NO_3)_2/HF/H_2O_2$ solution for 15 min. As the mc-Si comprises diverse crystal orientations, inverted pyramid arrays with varied orientations can be observed on the surface. We had pointed out that the anisotropic etching of CACE rose from the anisotropic deposition during the reaction.[25] In order to fully support this conjecture, polished (100) and (111) oriented c-Si with similar resistivity were immersed in the 5 mM $Cu(NO_3)_2$ and 4.6 M HF mixture at 50 °C. In the absence of H_2O_2, Cu^{2+} can be oxidized more easily, nucleate as a Cu atom and then grow into Cu NPs. Even in a very short time (20 s), the size of Cu NPs was much larger than that with H_2O_2 in the solution (Fig. 10b and c). Due to a higher surface dangling bond density, the Si (100) planes had more "available" electrons than Si (111). As a result, Cu^{2+} preferentially obtained electrons from Si (100), resulting in a larger density of Cu NPs on Si (100) than Si (111). The electroless deposition of Cu NPs accompanied by the oxidation and dissolution of the silicon beneath finally achieved the anisotropic etching of silicon.

Conclusions

The mechanisms of Cu NPs assisted chemical etching have been discussed here, as well as various phenomena during the etching, including the influence of the etchant, the doping type, the doping concentration and the original surface morphology of the silicon substrate. The charge transfer during the reaction is revealed by the simplified energy band diagram of the Si/$Cu(NO_3)_2/HF/H_2O_2$ system. The silicon conduction band provides electrons for the reduction of Cu^{2+} ions and H_2O_2 which on the other hand injects holes into the valence band of silicon through the deposited Cu NPs. The current density of the associated redox process shows high dependence on the electron density and oxidant concentration at the interface. The dynamic activity of Cu NPs, which depends on the concentration of the etchant, finally determines the surface morphology of silicon. In the case of inverted pyramid structures, the generation and dissolution of Cu NPs reach dynamic equilibrium. In addition, the etching rate of silicon by Cu assisted chemical etching is a combined effect of the electron concentration and defect density of the substrate, as well as the potential barrier at the interface of Si/Cu NPs. What's more, the electroless deposition of Cu NPs on Si (100) and Si (111) further verifies the anisotropic nature of Cu assisted chemical etching. In summary, the detailed mechanisms demonstrated in this paper will contribute to the controllable and reproducible fabrication of a low-cost micron-sized inverted pyramid texture for its application in the photovoltaic industry.

Acknowledgements

This work was supported by the Ministry of Science and Technology of the People's Republic of China (Grant No. 2011CB302002 and 2009CB929404), the National Natural Science Foundation of China (Grant No. 11174348, 51272280, 11274366, 61204067, and 61306011), the Chinese Academy of Sciences, and the Research Council of Norway in the framework of the IDEAS grant program administrated *via* the ENERGIX program, as well as the OXYDERA equipment grant from the Centre for Materials Science and Nanotechnology at the University of Oslo.

References

1 K. Q. Peng, Y. Xu, Y. Wu, Y. J. Yan, S. T. Lee and J. Zhu, *Small*, 2005, **1**, 1062–1067.
2 E. C. Garnett and P. D. Yang, *J. Am. Chem. Soc.*, 2008, **130**, 9224–9225.
3 V. Sivakov, G. Andra, A. Gawlik, A. Berger, J. Plentz, F. Falk and S. H. Christiansen, *Nano Lett.*, 2009, **9**, 1549–1554.
4 A. I. Hochbaum, R. K. Chen, R. D. Delgado, W. J. Liang, E. C. Garnett, M. Najarian, A. Majumdar and P. D. Yang, *Nature*, 2008, **451**, 163–167.
5 K. Peng, J. Jie, W. Zhang and S. T. Lee, *Appl. Phys. Lett.*, 2008, **93**, 033105.
6 B. H. Zhang, H. S. Wang, L. H. Lu, K. L. Ai, G. Zhang and X. L. Cheng, *Adv. Funct. Mater.*, 2008, **18**, 2348–2355.
7 L. L. Ma, Y. C. Zhou, N. Jiang, X. Lu, J. Shao, W. Lu, J. Ge, X. M. Ding and X. Y. Hou, *Appl. Phys. Lett.*, 2006, **88**, 171907.
8 S. K. Srivastava, D. Kumar, P. K. Singh, M. Kar, V. Kumar and M. Husain, *Sol. Energy Mater. Sol. Cells*, 2010, **94**, 1506–1511.
9 Z. P. Huang, N. Geyer, P. Werner, J. D. Boor and U. Gösele, *Adv. Mater.*, 2011, **23**, 285–308.
10 Y. P. Liu, T. Lai, H. L. Li, Y. Wang, Z. X. Mei, H. L. Liang, Z. L. Li, F. M. Zhang, W. J. Wang, A. Y. Kuznetsov and X. L. Du, *Small*, 2012, **9**, 1392–1397.
11 A. Kumagai, *Sol. Energy Mater. Sol. Cells*, 2015, **133**, 216–222.
12 X. G. Liu, P. R. Coxon, M. Peters, B. Hoex, J. M. Cole and D. J. Fray, *Energy Environ. Sci.*, 2014, **7**, 3223–3263.
13 F. Toor, J. B. Miller, L. M. Davidson, W. Duan, M. P. Jura, J. Yim, J. Forziati and M. R. Black, *Nanoscale*, 2016, **8**, 15448–15466.
14 J. Oh, H. C. Yuan and H. M. Branz, *Nat. Nanotechnol.*, 2012, **7**, 743–748.
15 A. Kraft, C. Wolf, J. Bartsch, M. Glatthaar and S. Glunz, *Sol. Energy Mater. Sol. Cells*, 2015, **136**, 25–31.
16 I. K. Filipek, F. Dross, K. Baert, J. L. Hernandez, S. Singh, K. V. Nieuwenhuysen and J. Poortmans, *Prog. Photovoltaics: Res. Appl.*, 2012, **20**, 350–355.
17 M. C. Putnam, D. B. Turner-Evans, M. D. Kelzenberg, S. W. Boettcher, N. S. Lewis and H. A. Atwater, *Appl. Phys. Lett.*, 2009, **95**, 163116.
18 K. Q. Peng, Y. J. Yan, S. P. Gao and J. Zhu, *Adv. Mater.*, 2002, **14**, 1164–1167.
19 K. Q. Peng, Y. Yan, S. Gao and J. Zhu, *Adv. Funct. Mater.*, 2003, **13**, 127–132.
20 K. Peng, J. Hu, Y. Yan, Y. Wu, H. Fang, Y. Xu, S. T. Lee and J. Zhu, *Adv. Funct. Mater.*, 2006, **16**, 387–394.
21 Z. P. Huang, N. Geyer, L. F. Liu, M. Y. Li and P. Zhong, *Nanotechnology*, 2010, **21**, 465301.
22 Y. T. Lu and A. R. Barron, *J. Mater. Chem. A*, 2014, **2**, 12043–12052.
23 F. Toor, J. Oh and H. M. Branz, *Prog. Photovoltaics: Res. Appl.*, 2015, **23**, 1375–1380.
24 Y. Cao, Y. R. Zhou, F. Z. Liu, Y. Q. Zhou, Y. Zhang, Y. Liu and Y. K. Guo, *ECS J. Solid State Sci. Technol.*, 2015, **4**, 331–336.
25 Y. Wang, L. X. Yang, Y. P. Liu, Z. X. Mei, W. Chen, J. Q. Li, H. L. Liang, A. Kuznetsov and X. L. Du, *Sci. Rep.*, 2015, **5**, 10843.
26 L. X. Yang, Y. P. Liu, W. Chen, Y. Wang, H. L. Liang, Z. X. Mei, A. Kuznetsov and X. L. Du, *ACS Appl. Mater. Interfaces*, 2016, **8**, 26–30.
27 A. Mavrokefalos, S. E. Han, S. Yerci, M. S. Branham and G. Chen, *Nano Lett.*, 2012, **12**, 2792–2796.
28 A. W. Smith and A. Rohatgi, *Sol. Energy Mater. Sol. Cells*, 1993, **29**, 37–49.
29 J. H. Zhao, A. H. Wang and M. A. Green, *Prog. Photovoltaics: Res. Appl.*, 1999, **7**, 471–474.
30 J. S. You, D. Kimb, J. Y. Huhb, H. J. Parkc, J. J. Pakc and C. S. Kanga, *Sol. Energy Mater. Sol. Cells*, 2001, **66**, 37–44.
31 K. Kumar, K. K. C. Lee, P. R. Herman, J. Nogami and N. P. Kherani, *Appl. Phys. Lett.*, 2012, **101**, 222106.
32 N. Chaturvedi, E. Hsiao, D. Velegol and S. H. Kim, *Nano Lett.*, 2011, **11**, 672–676.
33 H. H. Cheng, Y. Y. Chang, J. Y. Chu, D. Z. Lin, Y. P. Chen and J. H. Li, *Appl. Phys. Lett.*, 2012, **101**, 141113.
34 H. Zheng, M. G. Han, P. Zheng, L. Zheng, H. B. Qin and L. J. Deng, *Mater. Lett.*, 2014, **118**, 146–149.
35 K. Q. Peng, H. Fang, J. J. Hu, Y. Wu, J. Zhu, Y. J. Yan and S. T. Lee, *Chem. – Eur. J.*, 2006, **12**, 7942–7947.
36 J. Kim, Y. H. Kim, S. H. Choi and W. Lee, *ACS Nano*, 2011, **5**, 5242–5248.
37 N. Mitsugiz and K. Nagai, *J. Electrochem. Soc.*, 2004, **151**, G302–G306.
38 J. P. Lee, S. Choi and S. Park, *Langmuir*, 2011, **27**, 809–814.
39 B. M. Bang, H. Kim, J. P. Lee, J. Cho and S. Park, *Energy Environ. Sci.*, 2011, **4**, 3395–3399.
40 X. Zhong, Y. Q. Qu, Y. C. Lin, L. Liao and X. F. Duan, *ACS Appl. Mater. Interfaces*, 2011, **3**, 261–270.
41 W. Kern and D. A. Puotinen, *RCA Rev.*, 1970, **31**, 187–206.
42 J. Singh, *Semiconductor devices: basic principles*, Wiley, New York, 2001.
43 M. W. Jenkins, *J. Electrochem. Soc.*, 1977, **124**, 757–762.
44 M. S. Kulkarni, J. Libbert, S. Keltner and L. Muléstagno, *J. Electrochem. Soc.*, 2002, **149**, G153–G165.

